Nanoscale

COMMUNICATION

Cite this: *Nanoscale*, 2022, **14**, 617

Received 28th November 2021,
Accepted 11th December 2021

DOI: 10.1039/d1nr07836d

rsc.li/nanoscale

Controlling the nucleation and growth of ultrasmall metal nanoclusters with MoS_2 grain boundaries†

Yongliang Shi, ‡[a,b,c] Muztoba Rabbani,‡[d] Álvaro Vázquez-Mayagoitia,[e]
Jin Zhao [c,f,g] and Wissam A. Saidi *[d]

The stabilization of supported nanoclusters is critical for different applications, including catalysis and plasmonics. Herein we investigate the impact of MoS_2 grain boundaries (GBs) on the nucleation and growth of Pt NCs. The optimum atomic structure of the metal clusters is obtained using an adaptive genetic algorithm that employs a hybrid approach based on atomistic force fields and density functional theory. Our findings show that GBs stabilize the NCs up to a cluster size of nearly ten atoms, and with larger clusters having a similar binding to the pristine system. Notably, Pt monomers are found to be attracted to GB cores achieving 60% more stabilization compared to the pristine surface. Furthermore, we show that the nucleation and growth of the metal seeds are facile with low kinetic barriers, which are of similar magnitude to the diffusion barriers of metals on the pristine surface. The findings highlight the need to engineer ultrasmall NCs to take advantage of enhanced stabilization imparted by the GB region, particularly to circumvent sintering behavior for high-temperature applications.

Introduction

Ultrathin MoS_2 based substrates have been utilized as a support to disperse noble metal nanoclusters (NCs) for potential nanotechnology applications, including catalysis, plasmonics, and sensing.[1–9] For example, plasmonic Ag[10] and Au[11] nanoparticles on MoS_2 showed 10- to 20-fold enhanced photoluminescence; supported metal clusters on MoS_2 exhibited significantly enhanced H_2 conversion efficiency;[12–14] Ag/MoS_2 nanohybrids showed a seven-fold enhanced Raman scattering performance with potential in biomedical sensing applications;[15] and supported Au clusters on ultrathin MoS_2 nanosheets were used for comprehensive dual-modal imaging and photothermal–radiation combined therapy with effective treatment of tumors.[16] However, the fabrication of stable small NCs remains a significant challenge due to the weak interaction between the metal atoms and the support[17] that inevitably leads to NC sintering under realistic reaction conditions.[18]

Grain boundaries (GBs) are lattice imperfections that widely exist in 2D materials.[19] Furthermore, 2D materials offer unique opportunities to control and tune their GBs.[20] In MoS_2, several types of GBs have been characterized experimentally such as those associated with 5 and 7 atom rings and 5|7, 6|8, and 4|6 rings, in addition to 4 fold rings with point- and edge-sharing.[21–24] GBs can stabilize dopants and supported NCs as observed Pt NCs on graphene[25] and CeO_2,[26] and rare earth elements on Al_2O_3.[27] This is also the case in MoS_2 where a recent study reported that Pt atoms are drawn to dislocation sites in 6|4 and small-angle 5|8|5 GBs.[28] However, it is unknown how GBs impact the nucleation and growth of supported NCs compared to the defect-less substrate. Furthermore, it remains unclear whether there is a critical cluster size where the influence of the GB defect on the NC adsorption would be passivated. Central to these investigations is the ability to determine the lowest-energy configuration of the NCs on the substrate. Such investigations are generally complex, and even become more challenging in the presence of GBs considering the decrease in the symmetry of the surface sites.

---

[a] *Center for Spintronics and Quantum Systems, State Key Laboratory for Mechanical Behavior of Materials, School of Materials Science and Engineering, Xi'an Jiaotong University, Xi'an, Shaanxi 710049, China*
[b] *State Key Laboratory of Surface Physics and Department of Physics, Fudan University, Shanghai, 200433, China*
[c] *ICQD/Hefei National Laboratory for Physical Sciences at the Microscale, and CAS Key Laboratory of Strongly-Coupled Quantum Matter Physics, and Department of Physics, University of Science and Technology of China, Hefei, Anhui 230026, China*
[d] *Department of Mechanical Engineering and Materials Science, University of Pittsburgh, Pittsburgh, Pennsylvania 15261, USA. E-mail: alsaidi@pitt.edu*
[e] *Computational Science Division, Argonne National Laboratory, Lemont, IL, 60439, USA*
[f] *Department of Physics and Astronomy, University of Pittsburgh, Pittsburgh, PA 15260, USA*
[g] *Synergetic Innovation Center of Quantum Information & Quantum Physics, University of Science and Technology of China, Hefei, Anhui 230026, China*

† Electronic supplementary information (ESI) available. See DOI: 10.1039/d1nr07836d

‡ These authors contributed equally to this work.

Structure prediction at the nano level has been a long-standing challenge in atomistic simulations because the number of possible atomic arrangements is enormous and increases exponentially with the system size.[29,30] Previously, we have analyzed the nucleation and growth of Pt NCs on pristine $MoS_2(001)$, and elucidated the electronic and ground-state structures, energy landscapes and diffusion barriers, charge transfer, and possible kinetic limitations of the nucleation process. We find that the growth of the NCs transitions from 2D to 3D for NCs with $n = 5$ Pt atoms. In the 2D growth mode, the NCs attach to the $MoS_2(001)$ surface *via* the formation of Pt–Mo bonds, while as in the 3D case, the NCs form Pt–S bonds.[31] We also found that an adaptive genetic algorithm (AGA) is an effective approach to locate optimum structures of the NCs.[32] Namely, the structures identified by the AGA approach were validated atom-by-atom experimentally using *in situ* atom microscopy *via* a self-consistent approach.[32] These results in conjunction with the application of the AGA for structure prediction in bulk,[33] surface,[34,35] and interface[36,37] systems establish the veracity of our methodology.

Briefly, the AGA structural search combines the speed of classical potential with the accuracy of DFT.[38,39] Namely, the local optimization of new offsprings is performed using auxiliary classical atomistic potentials, which identify a selected number of structures screened further with DFT calculations. At the same time, DFT calculations will provide energies, forces, and stresses that are utilized to update the parameters of the classical potentials by a force-matching method.[40,41] This process is iterated up to a prescribed number of GA search cycles.

Here we explore the impact of grain boundary defects on the nucleation and growth of supported metal NCs of various sizes. We show that relatively small clusters are appreciably stabilized due to attractive interactions with the GB and particularly its core. However, we find that this stabilization diminishes as the NC increases in size. Namely, an NC with 20 Pt atoms is found to bind with an energy similar to that on a pristine surface. These studies highlight the need to engineer ultrasmall NCs to take advantage of the stabilization tendencies imported by the GB region particularly to circumvent sintering tendencies. Furthermore, we provide a deep understanding of Pt seed nucleation and growth pathways at different GB sites for MoS_2.

Results

Fig. 1a shows the structure of a pristine single-layer MoS_2 that consists of two hexagonal planes of S atoms that sandwich a hexagonal plane of Mo atoms. The Mo atoms have ionic-covalent interactions with the S atoms in a trigonal prismatic arrangement. In this study, we focus on the 5|7 ring GB that has been widely observed in MoS_2.[21,42] The 5|7 GB denoted by "⊥" has a Burgers vector $\mathbf{b} = (1,0)$ and is formed by combining two MoS_2 slabs with a 21° disorientation. Fig. 1b shows the atomic structure of the GB employed a nanoribbon model with a periodic direction along the GB direction. Thus, this model has only one GB, unlike the case with periodic boundary conditions that would result in two GBs in the model. As seen from the figure, we distinguish between three kinds of Mo and sulfur atoms: Mo_1 is located at the top of the five rings along [310]; Mo_2 is located at the boundary of the 5|7 ring; and Mo_3 is located at lower edge of the seven rings. As such, there are two sites of type Mo_2 and Mo_3 in the grain boundary region. A similar nomenclature is adapted for sulfur sites in Fig. 1b.

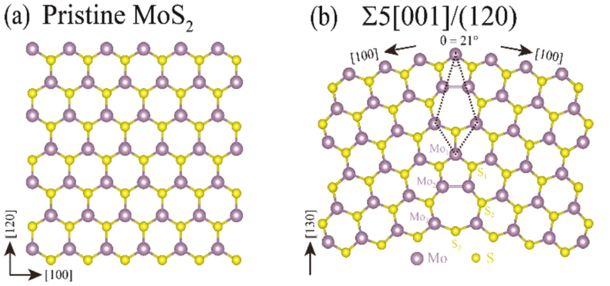

Fig. 1 (a) A substrate of the MoS_2 (001) surface with a supercell. (b) A nano ribbon (NR) model of the GB with an atomic structure of ⊥.

We employed the AGA approach to predict the structures of the supported NCs on the substrate. The rapid screening of the structures in this scheme is enabled using an embedded-atom method[43] potential as implemented in the Large-Scale Atomic/Molecular Massively Parallel Simulator (LAMMPS) code.[44] Density functional theory calculations are carried out using the Perdew–Burke–Ehrenzhof (PBE)[45] exchange–correlation functional and projector augmented wave (PAW) pseudopotentials implemented in the Vienna *Ab initio* Simulation Package (VASP).[46–48] For larger models, we have also carried out limited calculations using the real-space electronic structure method (RESCU) for computational efficiency.[49] More details about the computational setup are presented in the ESI.†

Below we briefly discuss the adsorption configurations for the NCs. The configurations for the Pt monomer are determined by investigating all adsorption sites near the GB. The reported adsorption energies are defined with respect to the energy of the isolated Pt atom E_{Pt} such that,

$$E_{BE} = \frac{1}{n}\left(E_{GB+Pt_n} - E_{MoS_2} - nE_{Pt}\right),$$

where n is the number of Pt atoms in the cluster, and E_{GB+Pt_n}/E_{MoS_2} are the energies of the substrate with/without NC. With this convention, the adsorption energies of the NCs are negative for stable configurations. For NCs with atoms less than four, the optimum cluster configurations are predicted using the smaller metallic clusters as motifs, especially those obtained at the monomer level. For larger NPs with $n \geq 4$, we employ the AGA to search for the energy minimum configurations. More detailed information about the atomic structures of the NCs is provided in the ESI.†

Pt_{1-3}@GB

Fig. 2(a–d) shows the most stable Pt monomer configurations with binding energies ranging from −4.57 to −2.75 eV per atom. The most preferential structure is the Pt atom at the hollow site of the 7-edge ring of the GB defect (h-$\perp_7$) having an energy of −4.57 eV per atom. For comparison, the most stable Pt monomer on pristine MoS_2 is atop of Mo with an adsorption energy of −2.83 eV per atom. The Pt monomer has the highest coordination at the hollow site that correlates with its high binding energy (see Table S1†). The second most stable adsorption is s-S_2 (Fig. 2b), with a binding energy of −3.45 eV per Pt. This configuration is similar to h-$\perp_7$ except that the positions of Pt and S_2 are exchanged. Inspired by the h-$\perp_7$ configuration that increasing the Pt coordination would result in more stabilization, the s-S_2 configuration is considered by displacing the S_2 atom from the t-Mo_3 configuration to create more bonds between the Pt monomer and the substrate. After relaxation, s-S_2 is more stable than t-Mo_3 by 0.51 eV. The third and fourth most stable adsorption configurations are t-Mo_3 and t-Mo_1 in Fig. 2c and d with binding energies of −2.94 eV per Pt and −2.75 eV per Pt, respectively. These configurations are similar to the atop Mo site on pristine MoS_2 and have similar binding energy. Importantly these local minima are essential for the monomer diffusion on the surface, as discussed later.

Fig. 2(e and f) shows three stable configurations for Pt_2. The most stable structure h-$\perp_7$-t-Mo_3 has a binding energy of −4.06 eV per Pt that is surprisingly lower than that of the monomer. For the Pt dimer, we investigated different combinations by positioning the two Pt atoms at the different sites identified from the monomer case. Because the h-$\perp_7$ site is energetically favorable, it is expected that the optimum configuration of Pt_2 will keep at least one monomer in the h-$\perp_7$ configuration and combining with another site. Our findings on the low energy dimer configurations are supportive of this. The two other structures, h-$\perp_7$-t-Mo_3 and h-$\perp_7$-$\perp_5$ (Fig. 2e and f) can also coexist as their energies are appreciably close to −4.06 eV per Pt.

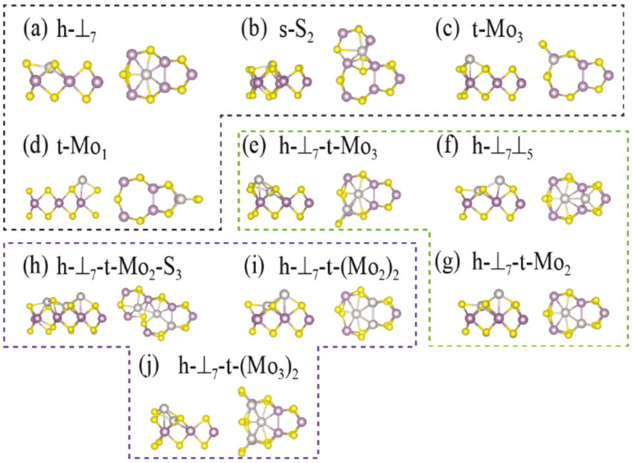

Fig. 2 Top and side views of the lowest-energy configurations for (a–d) Pt_1, (e–g) Pt_2, and (h–j) Pt_3. S, Mo, and Pt atoms are shown as yellow, purple and grey spheres, respectively.

We find several stable Pt_3 configurations with energies within ≈0.5 eV per atom. Fig. 2(h–j) shows the three lowest energy configurations with nearly equal energies ranging from −4.02 eV to −3.99 eV per Pt. The lowest-energy structure is h-$\perp_7$-t-Mo_2-S_3 (see Fig. 2h), which has two Pt atoms located at h-$\perp_7$ and t-Mo_2 similar to h-$\perp_7$-t-Mo_2 for the Pt_2 configuration.

Pt_{4-11}@B

Larger clusters have more complex atomic arrangements on the surface. We discuss here the most stable isomer. Pt_4 (Fig. 3a) adopts a bowl-like structure that is based on Pt_3 h-$\perp_7$-t-$(Mo_3)_2$ (Fig. 3c) with one more Pt located in the middle of Mo–Mo bonds. Importantly, Pt_4 is the largest planar cluster where all metal atoms are directly bonded to substrate atoms (mainly Mo). Pt_5 follows from Pt_3 h-$\perp_7$-t-Mo_2-S_3 (Fig. 2h) with one atom on top of the center atom and another one at a t-Mo_2 site. This is the first configuration that has two layers with the top layer having one Pt atom. Here, we see a sudden change in Pt–Mo and Pt–S bond lengths caused by the 2D to 3D change, where the Pt–S bond length decreased from 2.50 Å to 2.41 Å and the Pt–Mo bond length increased from 2.70 Å to 2.75 Å. The transition from 2D to 3D with the Pt_5 cluster was also observed in pristine MoS_2.

From Pt_6 to Pt_{11}, the binding energy of the most stable structures ranges from −4.10 eV to −4.19 eV per atom. For Pt_6, five atoms occupy different sites of the 7-fold ring. Pt_7 and Pt_8 are based on Pt_6 and just grow respectively by one Pt atom and two more Pt atoms located near S_3. The Pt_{10} and Pt_{11} structures can simply be divided into two layers. The first layer atoms are mostly bonded with S atoms except one atom bonded with the Mo_2 atom. The h-$\perp_7$ site is occupied in Pt_6–Pt_9 by one Pt atom while it is unoccupied in Pt_{10} and Pt_{11}. Due to this arrangement, the number of Pt–Mo bonds also decreases where Pt_{10} and Pt_{11} have only one Pt–Mo bond while Pt_6–Pt_9 have 3–6 bonds.

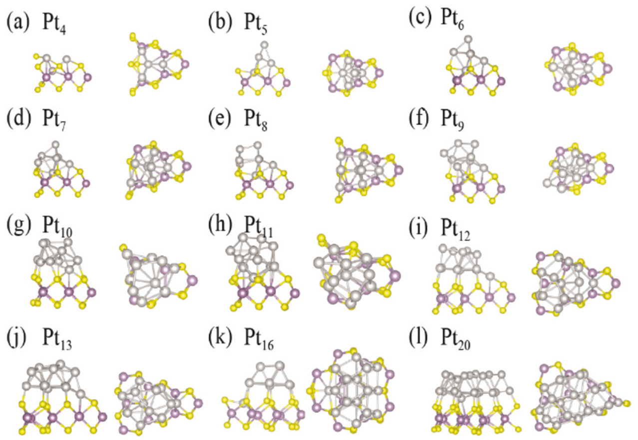

Fig. 3 Top and side views of the lowest-energy configurations from Pt_4 to Pt_{20}.

Pt_{12-20}@GB

For clusters larger than Pt_{11}, we note that some of the Pt atoms bond directly with the pristine surface atoms considering that all sites belonging to the GB region are occupied. Pt_{12}, Pt_{13}, Pt_{16}, and Pt_{20} have a two-layer structure, as shown in Fig. 3(i–l). The first layer Pt atoms are bonded mostly with S atoms except one atom bonded with Mo atoms. In Pt_{12} and Pt_{13}, one Pt atom is added to Mo_3 atoms while h-$\perp_7$ is unoccupied and in Pt_{16} but Pt_{20} one Pt atom occupies the h-$\perp_7$ site and no bonds with Mo_3 atoms. In Pt_{16}, the first and second layers contain ten and five atoms and are in close-packed stacking. The first layer contains ten atoms forming a hexagon lattice with two atoms in the center, and the top layer contains five atoms forming an isosceles trapezoid pattern. Pt_{20} also has two layers but is not a standard hexagonal close-packed stacking, and atoms in the top layer are not in the hollow position of the bottom layer. There are eleven atoms in the bottom layer and one atom on top of the t-Mo_3 site sink due to the topology of the GB defect. There are nine atoms in the second layer with three rows in the isosceles trapezoid pattern, and with two, three, and four atoms are atoms in each row.

Discussion

Fig. 4 shows the adsorption energies of the supported NCs and how these vary with the cluster size. Except for Pt_1, we find that the binding energy of the most stable NC configuration decreases with the increase of the cluster size. This trend is similar to what was previously observed on the pristine MoS_2 surface,[32] which is reproduced for convenience in Fig. 4. Furthermore, as seen from the figure, the NC binding energies on the GB structure are stronger than the corresponding values for the pristine surface. However, the extra stabilization of the NCs with the GB decreases as the NCs increase in size. For example, the Pt_1 binding energy on the pristine surface is −2.83 eV, while that on the GB structure is −4.57 eV per Pt. In contrast, the binding energy of Pt_{12} is −4.09 for the pristine surface and −4.23 eV per Pt on the GB.

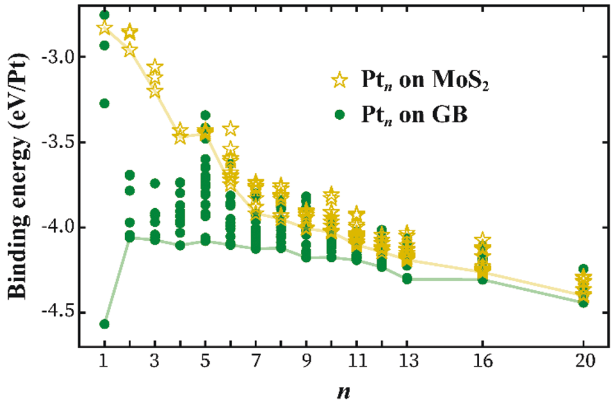

Fig. 4 Total binding energies ΔE_{BE} of the Pt_n cluster, which is normalized by the number of Pt atoms. The results of the pristine surface are reproduced from ref. 31 and 32. Lines connecting the lowest energy configurations serve as a guide to the eye.

Generally speaking, particle growth and nucleation result from the competition between metal-substrate interactions and the cohesive energy of metal clusters. The weak-anchoring force between the metal clusters and the substrate will drive particle agglomeration and the growth of 3D metal islands. Moreover, the roughness of the substrate, such as defects and GBs, will dramatically increase metal–substrate interactions. The size of the defect has also a high impact on the cluster growth. The reason for the enhanced interaction between the grain boundary and small-size quantum clusters can be traced back to the reactivity of the sites. Namely, GB cores are more reactive than surface sites due to bond saturation.

In agreement with the previous study of Pt NCs on pristine MoS_2,[31] we find that Pt_4 is the last planar structure as some Pt atoms start to occupy the top of the first metal layer for the larger clusters to form a 3D cluster instead of occupying substrate sites in a 2D configuration. With this transformation, the mechanism for the cluster attaching to the surface changes. For $n < 5$, Pt NCs directly bond with Mo sites. For the larger 3D metal clusters, all Pt atoms of the first layer bond with S instead, except one or two that still bond with the Mo site due to the restructuring of the MoS_2 substrate by the grain defect. This differs from the pristine substrate, where all Pt atoms for 3D structures corresponding to $n > 4$ are found to interact with sulfur. This 2D–3D transformation is due to complex competition between the formation of Pt–(S, Mo) and Pt–Pt bonds and bond strengths, which will be explained later.

One notable difference between MoS_2 and MoS_2/GB was found in the binding energy of Pt_1. On the pristine surface, we have always observed that the lower-sized cluster has smaller binding energy than the larger ones due to enhanced metal–metal interactions. However, Pt_1 on the GB has an anomalously considerable binding energy than Pt_2 and even that of Pt_{20}. While the Pt_{20} binding energy was 1.52 eV smaller than Pt_1 for the pristine surface, this is ~0.13 eV higher for the GB case. This anomalous stabilization of Pt_1 can be rationalized due to bond coordination and bond length. Namely, the h-$\perp_7$ configuration bonds with seven neighboring atoms in total within a bond-length cutoff of 2.95 Å and attain the shortest bond length of 2.66 Å.

To investigate the electronic/geometric origin of the defect-induced growth mechanism, we performed a comprehensive bond analysis using the LOBSTER package.[50] LOBSTER allows extracting precious bonding information from the plane-wave electronic wavefunctions by mapping onto a local basis.[51] For comparison, bond analysis on pristine MoS_2 is also included. All the bond analysis results are summarized in Fig. 5.

The crystal orbital overlap population (COOP) analysis provides a clear interpretation of the bonding and antibonding interactions in the electronic structure by identifying positive and negative orbital overlaps.[52] The integrated COOP (iCOOP) with all occupied energy levels can be utilized to define bonding and antibonding chemical bonds. The crystal-orbital Hamiltonian population (COHP)[53] method also provides valu-

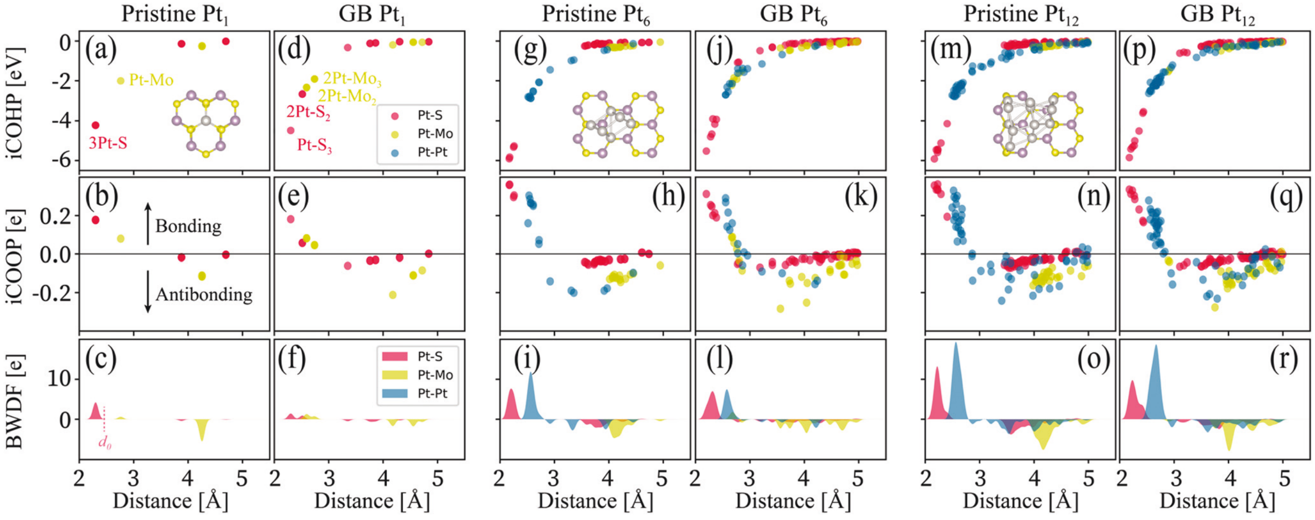

Fig. 5 Bond analysis of Pt_n (n = 1, 6, and 12) NCs on pristine and GB MoS_2 for all atomic pairs up to 5 Å. The first row (a, d, g, j, m, p) is an integrated COHP that serves as the first-principles measure of bond strength. The second row (b, e, h, k, n, q) is a scatterplot related to bond population into bonding and antibonding contributions. The third row (c, f, i, l, o, r) is the bond-weighted distribution function (BWDF) derived from all the data points in the corresponding plots shown in the second row.

able information as a bond strength indicator in energy contribution by integrating the COHP up to the Fermi level (thus, integrated COHP or iCOHP).[54] The COHP can be taken as the bond-weighted density of states where the bonding and antibonding contributions are positive and negative, respectively. Integration over all occupied levels, that is iCOHP, roughly provides bond contributions to the band-structure energy.

To explore how the GBs affect the configuration and growth mode of Pt NCs, we have calculated the iCOHP values for Pt–S, Pt–Mo, and Pt–Pt bonds for Pt_n (n = 1, 6, and 12) NCs, as shown in the first row of Fig. 5. To gain important insights, we have additionally performed this analysis on the Pt_n NCs on the pristine substrate from our previous work.[32] The more negative iCOHP values indicate that the bond is stronger and more covalent. In contrast, more positive values imply that the bonds are weaker and more polar.[55] First, the iCOHP of Pt–S is more negative than Pt–Pt bonds, which implies that Pt–S has larger bond strength than Pt–Pt. Thus, Pt atoms spattered on the MoS_2 surface prefer to form bonds with sulfur. Upon increasing the number of Pt atoms on the substrate, the number of Pt–Pt bonds also increases but much faster than the number of Pt–(Mo and S) bonds. For example, one Pt can form three Pt–S bonds at most, while Pt can have 12 homogeneous bonds in its face-centred cubic phase. This observation rationalizes the small critical atom number of Pt atoms required for 2D–3D transformation for both GB and pristine substrates. Second, Pt–Mo forms more metallic bonds with Pt_1@GB that are significantly more stable than Pt_1 on the pristine surface. As shown in Fig. 5a and d, Pt_1 has three Pt–S bonds both on the GB and pristine substrate while Pt_1@GB has two weaker Pt–S bonds than on the pristine case. However, Pt_1@GB has three more Pt–Mo bonds than on the pristine system. This implies that Mo-rich extended defects have the potential to control the size of Pt NCs by forming more metallic bonds. Third, only direct bonding atoms show strong attractive interaction. In contrast, long-range bonding corresponds to repulsive interactions except for a small part of bonding larger than 4 Å showing weak attractive interaction. As shown in the second row of Fig. 5, Pt–S and Pt–Pt bond lengths smaller than 3 Å correspond to bonding interaction, while larger bond lengths are antibonding and destabilize the system.

To further understand the iCOOP data in the second row of Fig. 5, we examine the "bond-weighted distribution function" (BWDF) with iCOOP,[56]

$$\mathrm{BWDF} = \sum_{\mathrm{AB}} \delta(r - |r_{\mathrm{AB}}|) \times \mathrm{iCOOP}.$$

The BWDF results are summarized in the third row of Fig. 5. The BWDF serves to define the bond length d_0 as the intersection point with the horizontal axes where the BWDF value goes to zero. When the bond length is smaller than d_0, the atomic interactions are attractive, while when the bond length is larger than d_0, they are repulsive. The results show clearly the role played by the direct bonding of Pt–Mo and Pt–S on the growth mode of NCs. Finally, the third row of Fig. 5 shows a clear increase in the Pt–Pt bond contribution while the bond strengths of Pt–Mo and Pt–S do not appreciably change. This explains why the larger Pt NCs show similar binding strengths on the GB and pristine substrate, as shown in Fig. 4.

To examine the long-term thermal stability of the predicted Pt clusters, we performed *ab initio* molecular dynamics simulation at 300 K for the most stable configuration of Pt_1, Pt_6 and Pt_{12}, as shown in Fig. S1.† No structural transition is observed after 3 ps. These results suggest that the NPs are stable and can be observed experimentally.

Our discussions thus far emphasized the thermodynamic stability of the clusters and particularly the enhanced stability of the monomer and dimer configurations. However, the mobility due to thermal hopping plays an essential role in the early stages of NC growth. It is not apparent whether large kinetic barriers prevent their nucleation in the GB core due to stronger repulsive interactions with the boundary region. For example, on the CeO$_2$(111) surface, the Au atom has a clear thermodynamic preference to occupy the oxygen vacancies, but a large kinetic barrier prohibits this process.[57]

To understand diffusion processes on the MoS$_2$ surface and focus mainly on the region near the GB core, we constructed a slice for the potential energy surface (PES) for a Pt monomer as it diffuses from one hollow site h-$\perp_7$ to a neighboring hollow site h-$\perp'_7$. Here we used a 2 × 1 × 1 supercell of the structure in Fig. 1b, thus including two GB cores that are distinguished between each other using the prime notation. The diffusion process is shown schematically in Fig. 6a.

The PES is constructed using nudged elastic band (NEB) calculations assuming different trajectories connecting the identified local minima (see Fig. 6). As seen in the figure, there are three local minima t-Mo$_3$, h-S, and t-Mo$_1$ with energies 1.7, 2.2, and 2.2 eV with respect to h-$\perp_7$. The overall activation energy for this diffusion process is 2.7 eV, suggesting that once Pt occupies h-$\perp_7$ it becomes practically immobile. For comparison, the activation energy for hopping between two t-Mo sites on the pristine surface is 0.6 eV.

The constructed PES in Fig. 6 sheds light also on the initial nucleation process of the monomer at the GB. As Pt atoms attach to the MoS$_2$ substrate, there is a minimal possibility that these would directly adsorb in the GB core region due to its negligible surface area. Instead, Pt atoms will randomly occupy surface sites such as t-Mo based on the PES of the pristine surface. Given the relatively small ~0.6 eV activation energy for monomer diffusion on the pristine surface,[58] such Pt atoms located initially far from the GB site can diffuse to the GB region. We have verified that the monomer diffusion from the t-Mo site to t-Mo$_3$ or t-Mo$_1$ site has a 0.6 eV that coincides with that of diffusion in the pristine system. Next, we investigated the diffusion from the t-Mo$_3$ and t-Mo$_1$ sites to h-$\perp_7$. From the PES in Fig. 6a, we see that the diffusion barrier from t-Mo$_3$ to h-$\perp_7$ is only 0.1 eV. From t-Mo$_1$, Pt needs an activation energy of ~0.9 eV to reach h-$\perp'_7$ as it diffuses through two nearby hollow sites. On the other hand, the diffusion from t-Mo$_1$ to h-$\perp_7$ has a 0.4 eV barrier to reach h-S first and then a 0.1 eV barrier to t-Mo$_3$.

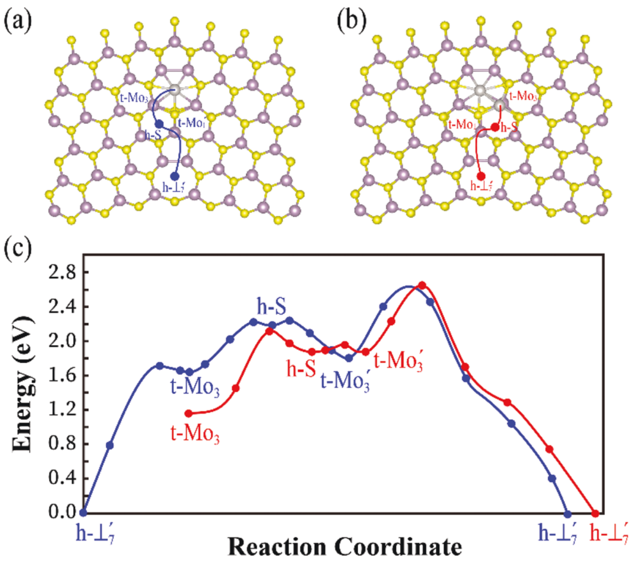

Fig. 6 Schematic pathways of Pt (a) monomer and (b) dimer diffusion along the GB. The positions of local minima are marked. (c) The energy profile along the two pathways in (a) and (b). The blue (red) line corresponds to Pt$_1$ (Pt$_2$).

The above analyses suggest that Pt atom nucleation at the grain boundary core is facile based on thermodynamic and kinetic considerations. To further understand how frequently this diffusion will occur, we calculate the hopping event per second using transition-state theory (TST, $k = \nu_0 e{-}^{\Delta E/k_B T}$ where $\nu_0 = 10^{13}$ s^{-1} is the rate prefactor assumed to be a constant, which is on the order of atomic vibration frequency corresponding to the unstable mode in the transition state mode,[59] ΔE is the activation energy, k_B is the Boltzmann constant, and T is room temperature. The hopping rate from t-Mo to t-Mo$_3$ or t-Mo$_1$ is ≈10 s^{-1} as for the hopping rate between two t-Mo sites on the pristine surface. Furthermore, the GB site hopping from t-Mo$_3$ to h-$\perp_7$ is 10^{11} s^{-1}. Finally, from t-Mo$_1$ to h-$\perp_7$ in two different pathways will have either 10^6 or 10^{-1} hopping per second at room temperature. Therefore, we conclude that Pt nucleation on the GB is limited by metal diffusion on the surface.

Furthermore, we examined kinetic barriers associated with the formation and dissociation of the Pt dimer configuration. Here we start from the most stable configuration h-$\perp_7$-t-Mo$_3$ of Pt$_2$. Fig. 6b shows a schematic of the diffusion path. From the PES in Fig. 6c (red curve), a Pt atom located at t-Mo$_1$ requires an activation energy of 0.2 eV to diffuse to the Mo$_3$ site and attach to the Pt monomer located at h-$\perp_7$. On the other hand, the PES shows that the dimer requires an activation energy of 1.0 eV to diffuse to t-Mo$_1$ and then an activation energy of 0.7 eV to diffuse to h-$\perp'_7$. Thus, the formation of the Pt$_2$ dimer requires a barrier of ~0.2 eV, while its dissociation requires a barrier of 1 eV. Similar to the Pt nucleation, the growth of Pt$_2$ at the GB core is also limited by the diffusion of metal on the surface.

Almost all experimental studies, *e.g.* ref. 25, 27, 28 and 54, show that metal clusters favor the nucleation and growth in the GB region, which has led to the shared recognition that GBs' imparted stabilization is general to any cluster size. Our results clearly show that the impact of a single GB on the NC stabilization is size-dependent, where it is only enhanced for clusters with nearly ten atoms on the MoS$_2$ support. Hence, thermodynamically, larger NCs are as easily dislodged in whole from a GB region as from a pristine region. However, in agreement with experimental studies, we also find that the GBs are the preferable nucleation centers of the metal particles, resulting in having the larger clusters growing in the GB region. We posit that these findings provide a new pathway to synthesis, particularly for high-performance catalysts at elevated temperatures.

To extend our results to other types of GB, we explore the interaction of Pt with the Mo-rich dislocation cores of 5|8|5 and 6|4, which were reported before.[28] We constructed the same dislocation cores as in ref. 28 but using periodic models, as shown in Fig. S2.† The adsorption configurations of the Pt monomer are shown in Fig. 7a and b. There are four 4-coordinated Mo atoms in the 5|8|5 dislocation core. The distinct difference between 5|8|5 and 6|4 is that a S_0 pair is present in the center of four 4-coordinated Mo atoms, as shown in Fig. S2.† The most energetically favored site is the hollow site of 5|8|5, as shown in Fig. 7a, which is in line with ref. 28. Also, Pt_1@6|4 shown in Fig. 7b is found to be more stable than the configuration reported in ref. 28. The increased Pt coordination compared to the pristine substrate leads to more stabilization, just like the aforementioned s-S_2 configuration on the 5|7 dislocation core. The Pt atom in the 6|4 core displaces the S_0 atom and forms two Pt–Mo and Pt–S bonds. The Pt monomer strongly interacts with 5|8|5 and 6|4 GBs with binding energies of −7.99 eV and −4.75 eV, respectively, as shown in Table S3.† We note that the values reported before were −1.64 and 2.11 eV as these values were measured with respect to bulk Pt and not to single-atom Pt, as done in the present study.[28] Therefore, the strong adsorption of the monomer system with the GB defect is general and applies to other MoS_2 GBs, suggesting that GB engineering could effectively stabilize ultrasmall NCs or single-atom catalysts.[60,61] We note that typically, the edge of MoS_2 is the only active site. Here, we propose that GBs and metal atom combinations can activate the basal plane and result in a more significant number of active catalytic sites. The optimal combination needs further experimental verification.

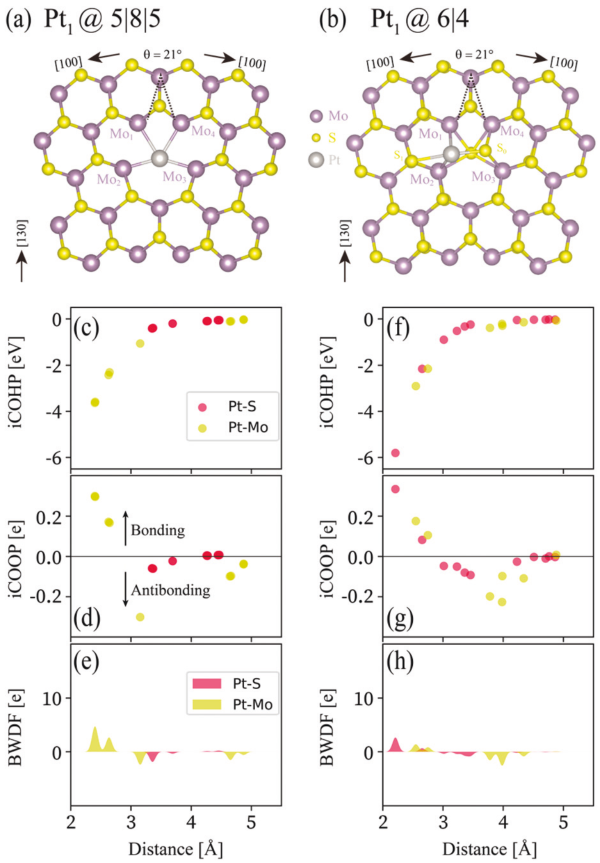

Fig. 7 Top views of the lowest energy configurations for (a) Pt_1 @ 5|8|5 and (b) Pt_1 @ 6|4. (c–e) and (f–h) are the corresponding bond analysis results similar to Fig. 5.

We make a comprehensive bond analysis to understand further the strong bonding between the Pt monomer and the dislocation cores of 5|8|5 and 6|4, as shown in Fig. 7c–h. We draw the following conclusions. First, for the Pt monomer in the 5|8|5 core, Pt–Mo bonds can be grouped into two types. One type is with a bond length of 2.40 Å, such as Pt–Mo_2 and Pt–Mo_3, which have the shortest Pt–Mo bond length in this report. Hence, these have the strongest Pt–Mo bonding interaction with iCOHP energy ∼ −5.8 eV. These results rationalize the large binding energy compared to the pristine systems. The other type is with a bond length of 2.64 Å, such as Pt–Mo_1 and Pt–Mo_4, which have a smaller iCOHP energy of ∼−2.4 eV. Second, we note from the figure that only Pt–Mo bonds are in bonding interactions, confirming the vital role of exposed Mo atoms, as shown in Fig. 7d. This shares the same mechanism with the aforementioned 5|7 dislocation core. Third, for the Pt monomer in the 6|4 core, two Pt–S and two Pt–Mo bonds are formed, all are bonding interactions, as shown in Fig. 7g. However, a strong Pt–S_0 bond with an ICOHP energy of −5.8 eV, the considerable deformation energy of MoS_2 makes an energy penalty to the total binding energy. Finally, the 5|8|5 and 6|4 cores are larger extended defects than the 5|7 core. Hence, we expect that these GB cores can stabilize larger metal NCs.

Conclusions

We have presented a comprehensive theoretical study of the atomic structure of stable NCs on the MoS_2 substrate with a grain boundary defect. We have applied an adaptive genetic approach employing classical force fields and density functional theory calculations to obtain the lowest energy structures. The GB increases the stability of Pt_1–Pt_{12} clusters, although with enhancements that decrease with the cluster size. We showed that GB effects are passivated for NCs with more than 13 Pt atoms, and the GBs stabilize the NCs similar to the pristine system. In particular, we show that the GB can stabilize a Pt monomer 65% more than the pristine surface, suggesting that this system is of great potential as a single atom catalyst. The monomer and dimer are found to nucleate at the GB core easily with rates that are only limited by the diffusion of the metal atoms on the surface. Furthermore, we showed that the nucleated monomers and dimers at the GB are protected against dissociations by relatively larger barriers of 1.7 and 1 eV, respectively. To mitigate the NC's sintering behaviour for high-temperature applications, our findings highlight the need to carefully design the size of the NCs to increase their stability or to increase the surface roughness of the substrate to stabilize the clusters with more than one grain boundary.

Our findings are general for other grain boundary types in MoS_2 or for other systems. We expect the size dependence associated with stabilization enhancements of supported metal clusters with GBs to be a general concept that applies to other defects. Furthermore, we expect the critical cluster size for defect passivation to depend on the defect type. For instance, with sulfur vacancies, we expect clusters with less than 12 atoms to be equally stable as on the pristine surface, given that effects of S vacancies are more localized than those of GBs. On the other hand, for the 5|8|5 and 6|4 GB cores, we expect the opposite as these dislocation cores are more extended than the 5|7 one.

Author contributions

W. A. S. conceived the idea and designed the research. Y. S. carried out the theoretical calculations. Y. S. and M. R. wrote the manuscript. All authors discussed the results and commented on the paper.

Conflicts of interest

There are no conflicts to declare.

Acknowledgements

W. A. S. and M. R. acknowledges the financial support from the National Science Foundation (Award No. DMR-1809085). Y. S. acknowledges the support of the National Natural Science Foundation of China (NSFC), grant no. 11904353 and the Open Project of State Key Laboratory of Surface Physics, grant no. KF2020_10 Sciences (Ministry of Education). J. Z. acknowledges the support of the National Key Foundation of China, Department of Science and Technology, grant no. 2017YFA0204904 and 2016YFA0200604 and the NSFC, grant no. 11974322 and 11620101003. Calculations were performed at the Argonne Leadership Computing Facility, a DOE Office Science User Facility supported under Contract DE-AC02-06CH11357, and the Supercomputing Center at USTC. Y. S. gratefully acknowledges HZWTECH for providing computation facilities.

References

1 X. Huang, Z. Zeng, S. Bao, M. Wang, X. Qi, Z. Fan and H. Zhang, *Nat. Commun.*, 2013, **4**, 1444.

2 A. V. Akimov, A. J. Neukirch and O. V. Prezhdo, *Chem. Rev.*, 2013, **113**, 4496–4565.

3 Z. L. He and W. X. Que, *Appl. Mater. Today*, 2016, **3**, 23–56.

4 F. Zheng, L. Huang, L.-W. Wong, J. Han, Y. Cai, N. Wang, Q. Deng, T. H. Ly and J. Zhao, *Adv. Sci.*, 2020, **7**, 2001742.

5 H. Wang, Z. Lu, S. Xu, D. Kong, J. J. Cha, G. Zheng, P.-C. Hsu, K. Yan, D. Bradshaw, F. B. Prinz and Y. Cui, *Proc. Natl. Acad. Sci. U. S. A.*, 2013, **110**, 19701–19706.

6 Z. Huang, G. Hao, C. He, H. Yang, L. Xue, X. Qi, X. Peng and J. Zhong, *J. Appl. Phys.*, 2013, **114**, 083706.

7 T. H. M. Lau, J. S. Foord and S. C. E. Tsang, *Nanoscale*, 2020, **12**, 10447–10455.

8 X. Li, Y. Zhang, J. Zhang and C. Wang, *Nanoscale*, 2019, **11**, 23110–23115.

9 Z. H. Wei and S. Zhuiykov, *Nanoscale*, 2019, **11**, 15709–15738.

10 S. Butun, S. Tongay and K. Aydin, *Nano Lett.*, 2015, **15**, 2700–2704.

11 S. Diefenbach, E. Parzinger, J. Kiemle, J. Wierzbowski, S. Funke, B. Miller, R. Csiki, P. Thiesen, A. Cattani-Scholz, U. Wurstbauer and A. W. Holleitner, *J. Phys. Chem. C*, 2018, **122**, 9663–9670.

12 X. Huang, Z. Zeng, S. Bao, M. Wang, X. Qi, Z. Fan and H. Zhang, *Nat. Commun.*, 2013, **4**, 1444.

13 J. Kim, S. Byun, A. J. Smith, J. Yu and J. Huang, *J. Phys. Chem. Lett.*, 2013, **4**, 1227–1232.

14 S. Zhao, R. Jin, Y. Song, H. Zhang, S. D. House, J. C. Yang and R. Jin, *Small*, 2017, **13**, 1701519.

15 P. Zuo, L. Jiang, X. Li, B. Li, P. Ran, X. Li, L. Qu and Y. Lu, *ACS Sustainable Chem. Eng.*, 2018, **6**, 7704–7714.

16 T. Liu, S. Shen, Y. Huang, X. Zhang, Z. Lai, T. H. Tran, Z. Liu and L. Cheng, *Nanoscale*, 2019, **11**, 22788–22795.

17 H. F. Lv, Z. Xi, Z. Z. Chen, S. J. Guo, Y. S. Yu, W. L. Zhu, Q. Li, X. Zhang, M. Pan, G. Lu, S. C. Mu and S. H. Sun, *J. Am. Chem. Soc.*, 2015, **137**, 5859–5862.

18 C. Z. Wen, Q. H. Hu, Y. N. Guo, X. Q. Gong, S. Z. Qiao and H. G. Yang, *Chem. Commun.*, 2011, **47**, 6138–6140.

19 W. J. Zhou, D. M. Hou, Y. H. Sang, S. H. Yao, J. Zhou, G. Q. Li, L. G. Li, H. Liu and S. W. Chen, *J. Mater. Chem. A*, 2014, **2**, 11358–11364.

20 Y. Wang and V. H. Crespi, *Nano Lett.*, 2017, **17**, 5297–5303.

21 W. Zhou, X. Zou, S. Najmaei, Z. Liu, Y. Shi, J. Kong, J. Lou, P. M. Ajayan, B. I. Yakobson and J.-C. Idrobo, *Nano Lett.*, 2013, **13**, 2615–2622.

22 A. M. van der Zande, P. Y. Huang, D. A. Chenet, T. C. Berkelbach, Y. You, G.-H. Lee, T. F. Heinz, D. R. Reichman, D. A. Muller and J. C. Hone, *Nat. Mater.*, 2013, **12**, 554–561.

23 X. Zou, Y. Liu and B. I. Yakobson, *Nano Lett.*, 2013, **13**, 253–258.

24 N. Gao, Y. Guo, S. Zhou, Y. Bai and J. Zhao, *J. Phys. Chem. C*, 2017, **121**, 12261–12269.

25 K. Kim, R. W. Johnson, J. T. Tanskanen, N. Liu, M.-G. Kim, C. Pang, C. Ahn, S. F. Bent and Z. Bao, *Nat. Commun.*, 2014, **5**, 4781.

26 G. Zhou, P. Li, Q. Ma, Z. Tian and Y. Liu, *Nano Lett.*, 2018, **18**, 1668–1677.

27 J. Buban, K. Matsunaga, J. Chen, N. Shibata, W. Ching, T. Yamamoto and Y. Ikuhara, *Science*, 2006, **311**, 212–215.

28 S. Wang, H. Sawada, X. Han, S. Zhou, S. Li, Z. X. Guo, A. I. Kirkland and J. H. Warner, *ACS Nano*, 2018, **12**, 5626–5636.

29 M. John, *Nature*, 1988, **335**, 201–201.

30 Y. Guo, Y. Wei, H. Li and T. Zhai, *Small*, 2017, **13**, 1701649.

31 W. A. Saidi, *Cryst. Growth Des.*, 2015, **15**, 642–652.

32 Y. Shi, B. Song, R. Shahbazian-Yassar, J. Zhao and W. A. Saidi, *J. Phys. Chem. Lett.*, 2018, **9**, 2972–2978.

33 X. Zhao, M. C. Nguyen, W. Y. Zhang, C. Z. Wang, M. J. Kramer, D. J. Sellmyer, X. Z. Li, F. Zhang, L. Q. Ke, V. P. Antropov and K. M. Ho, *Phys. Rev. Lett.*, 2014, **112**, 045502.

34 Y. Shi, H. Sun, M. C. Nguyen, C. Wang, K. Ho, W. A. Saidi and J. Zhao, *Nanoscale*, 2017, **9**, 11553–11565.

35 Y. Shi, H. Sun, W. A. Saidi, N. Manh Cuong, C. Z. Wang, K. Ho, J. Yang and J. Zhao, *J. Phys. Chem. Lett.*, 2017, **8**, 1764–1771.

36 Y. Wang, Y. Shi, C. Zhao, Q. Zheng and J. Zhao, *Phys. Rev. B*, 2019, **99**, 165309.

37 X. Zhao, Q. Shu, M. C. Nguyen, Y. Wang, M. Ji, H. Xiang, K.-M. Ho, X. Gong and C.-Z. Wang, *J. Phys. Chem. C*, 2014, **118**, 9524–9530.

38 M. Ji, K. Umemoto, C.-Z. Wang, K.-M. Ho and R. M. Wentzcovitch, *Phys. Rev. B: Condens. Matter Mater. Phys.*, 2011, **84**, 220105–220105.

39 S. Q. Wu, K. Umemoto, M. Ji, C. Z. Wang, K. M. Ho and R. M. Wentzcovitch, *Phys. Rev. B: Condens. Matter Mater. Phys.*, 2011, **83**, 184102.

40 P. Brommer and F. Gahler, *Modell. Simul. Mater. Sci. Eng.*, 2007, **15**, 295–304.

41 A. Banerjea and J. R. Smith, *Phys. Rev. B*, 1988, **37**, 6632–6645.

42 A. M. Van Der Zande, P. Y. Huang, D. A. Chenet, T. C. Berkelbach, Y. You, G.-H. Lee, T. F. Heinz, D. R. Reichman, D. A. Muller and J. C. Hone, *Nat. Mater.*, 2013, **12**, 554–561.

43 M. I. Baskes, *Phys. Rev. Lett.*, 1987, **59**, 2666–2669.

44 S. Plimpton, *J. Comput. Phys.*, 1995, **117**, 1–19.

45 J. P. Perdew, K. Burke and M. Ernzerhof, *Phys. Rev. Lett.*, 1996, **77**, 3865–3868.

46 G. Kresse and J. Hafner, *Phys. Rev. B: Condens. Matter Mater. Phys.*, 1994, **49**, 14251–14269.

47 G. Kresse and J. Hafner, *Phys. Rev. B: Condens. Matter Mater. Phys.*, 1993, **48**, 13115–13118.

48 G. Kresse and J. Hafner, *Phys. Rev. B: Condens. Matter Mater. Phys.*, 1993, **47**, 558–561.

49 V. Michaud-Rioux, L. Zhang and H. Guo, *J. Comput. Phys.*, 2016, **307**, 593–613.

50 S. Maintz, V. L. Deringer, A. L. Tchougreeff and R. Dronskowski, *J. Comput. Chem.*, 2016, **37**, 1030–1035.

51 S. Maintz, V. L. Deringer, A. L. Tchougréeff and R. Dronskowski, *J. Comput. Chem.*, 2013, **34**, 2557–2567.

52 T. Hughbanks and R. Hoffmann, *J. Am. Chem. Soc.*, 1983, **105**, 3528–3537.

53 R. Dronskowski and P. E. Bloechl, *J. Phys. Chem.*, 1993, **97**, 8617–8624.

54 A. L. Görne and R. Dronskowski, *Carbon*, 2019, **148**, 151–158.

55 V. L. Deringer, A. L. Tchougreeff and R. Dronskowski, *J. Phys. Chem. A*, 2011, **115**, 5461–5466.

56 V. L. Deringer, W. Zhang, M. Lumeij, S. Maintz, M. Wuttig, R. Mazzarello and R. Dronskowski, *Angew. Chem., Int. Ed.*, 2014, **53**, 10817–10820.

57 P. G. Lustemberg, Y. Pan, B. J. Shaw, D. Grinter, C. Pang, G. Thornton, R. Pérez, M. V. Ganduglia-Pirovano and N. Nilius, *Phys. Rev. Lett.*, 2016, **116**, 236101.

58 H. Li, S. Wang, H. Sawada, G. G. D. Han, T. Samuels, C. S. Allen, A. I. Kirkland, J. C. Grossman and J. H. Warner, *ACS Nano*, 2017, **11**, 3392–3403.

59 M. Mantina, Y. Wang, R. Arroyave, L. Q. Chen, Z. K. Liu and C. Wolverton, *Phys. Rev. Lett.*, 2008, **100**, 215901.

60 C. Zhu, S. Fu, Q. Shi, D. Du and Y. Lin, *Angew. Chem., Int. Ed.*, 2017, **56**, 13944–13960.

61 B. Qiao, A. Wang, X. Yang, L. F. Allard, Z. Jiang, Y. Cui, J. Liu, J. Li and T. Zhang, *Nat. Chem.*, 2011, **3**, 634–641.